Reverse wavefront engineering for remote generation of a near-infrared femtosecond Bessel beam filament in air

Long Zou [1,2] Chen Sun,[1] Yunfei Rao [1] Tianyang Sun,[1] Jin Yu [1,*] and Arnaud Couairon[2,†]
[1]*School of Physics and Astronomy, Shanghai Jiao Tong University, 200240 Shanghai, China*
[2]*CPHT, CNRS, Ecole Polytechnique, Institut Polytechnique de Paris, F-91128 Palaiseau, France*

(Received 13 July 2022; accepted 27 September 2022; published 12 October 2022)

Precise control of the filamentation of an ultrashort and intense near-infrared laser pulse in air is crucial for many applications but remains challenging. By combining inverse design for shaping of a pulse at the output of a laser with simulation of the nonlinear propagation of the pulse in air, we numerically investigate the way to simultaneously control the length and position of a plasma filament at an arbitrary remote distance for the first time. An intermediate state, with a Bessel-Gauss beam profile, is introduced between the laser output and the filament. Through forward and backward propagations of the intermediate state, an end-to-end design of the initial laser pulse is achieved to match the desired filament characteristics. Our calculations show that a properly engineered torus pulse can project such a Bessel-Gauss beam at remote distance and generate a long plasma filament without requiring any feedback loop. We also proposed an experimental arrangement to project such an intermediate state and generate the corresponding filament remotely. The method can be further extended to other types of filaments or targets that may be reached from different intermediate states.

DOI: 10.1103/PhysRevResearch.4.043025

I. INTRODUCTION

The discovery of the nonlinear propagation of an intense femtosecond laser pulse in air in the form of a filament in 1995 [1] has opened a new era of atmospheric applications of ultrashort laser pulses [2]. The ability of an ultrashort and intense laser pulse to propagate over an outstandingly extended distance due to a competition among diffraction, nonlinear focusing, and plasma generation [3,4], has enabled applications so far unthinkable, such as supercontinuum white-light lidar [2,5–7], lightning triggering and guiding [8–13], virtual antennas [14], terahertz emission from a remote plasma source [15–17], and laser-induced breakdown spectroscopy detection and analysis of a target at a large distance [18–20].

Further implementations of and full benefits from the demonstrated applications crucially rely on the capacity to control filaments, with respect to their most important characteristics, the starting distance, length, optical intensity, as well as electron density in the associated plasma channels. Research efforts in the generation, characterization, and optimization of filaments at a remote distance and over a large extent in the atmosphere have been conducted intensively over the last two decades, highlighted notably by an observation of vertical propagation at an altitude of 20 km, of the supercontinuum white light generated by filaments formed at a distance estimated at 2 km above the laser [21], and a direct evidence of plasma channels associated to filaments horizontally propagating at a distance exceeding 1 km from the laser [22]. Simple waveform and wavefront modulations of the output pulses of a CPA laser by respectively group velocity dispersion (GVD) precompensation and beam collimation by telescope were applied in to push the filament starting position to the largest possible distance [23–25]. Air pressure has also been found to affect the onset of filament; however, its length is almost invariant [26–28]. More recent experimental as well as theoretical efforts have been focused on the generation of long and stable laboratory scale filaments. Wavefront reshaping was introduced using a deformable mirror [29,30] and optimized by a genetic algorithm [31] to increase the filament length and control the filament pattern with an optimized manipulation of the energy reservoir [32]. The model of an energy reservoir surrounding and dynamically replenishing a filament [32] has inspired other works, demonstrating the prevailing role of nonlinear losses in the robustness of filaments, acting as a sink of energy in the high intensity core of the beam and driving a conical energy flux from the low intensity tails that refills and sustains the filament [33–36]. A spontaneous emergence of such energy flux toward the filament is exemplified by the nonlinear propagation of a Bessel-Gauss beam showing an effectiveness in generating a long and stable filament in spite of nonlinear losses [37–40]. An approach with a Gaussian beam surrounded in a suitable way, by a ring auxiliary beam, leads to a significant protraction of the filament length [41,42]. A similar physical process relying on the nonlinear propagation of Bessel-Gauss beams, albeit in the tight focusing regime, was applied to generate long aspect ratio plasma channels in the bulk of dielectric media.

*jin.yu@sjtu.edu.cn
†arnaud.couairon@polytechnique.edu

Their subsequent evolution into void through channels [43] presents a significant interest for micromachining applications [44–48].

While projecting a near-infrared (NIR) filament system to a remote distance in the atmosphere and keeping it to survive over a large extent beyond the nonlinear focus seem to be fundamentally challenged by nonlinear losses owing to the appearance of a plasma channel [3], solutions have been proposed and demonstrated for mid-infrared and long-wavelength infrared pulses with new collapse-arresting mechanisms allowing a low-loss and filamentary propagation over a large distance [49,50].

In this paper, we implement an approach of wavefront engineering by inverse design in order to delay and stretch the effect of nonlinear losses while launching a NIR filament to a larger distance. The approach is based on the possibility that a well-defined wavefront called intermediate state can be projected to an arbitrarily large distance with a negligible loss. The subsequent evolution of the system leads to a filament associated with a uniform and stable plasma string. The wavefront of the initial pulse at the output of a CPA laser can be found by reversely propagating the intermediate pulse toward the laser, with a practical constraint that the resulting wavefront can be prepared using a reasonably accessible optical arrangement. For linear propagation, the feasibility of the procedure is guaranteed by the optical reversibility [51]. For an ultrashort intense laser pulse undergoing filamentation with a significant ionization loss, the reversibility has been expressly demonstrated to be valid for specific wavefronts [52]. However, as mentioned in Ref. [53], *the reversibility ensures neither that any arbitrary pulse shape can readily be backpropagated, nor that it will follow a filamentary path during its backpropagation.* For an arbitrary wavefront, the nonlinear loss, being turned into a gain for backward propagation, may indeed lead to a divergence of the simulation. Berti *et al.* proposed an elegant strategy to overcome this problem, based on backpropagation of a hybrid laser pulse that combines a post-filamented pulse with a target waveform, allowing the synthesis of a waveform in the postfilament region, with desired features for a specific application [53]. In the present paper, rather than reaching a specific waveform at a given distance after a filament, our goal is to control the features of the target pulse that will subsequently undergo filamentation over a predefined length. Therefore, in our numerical simulation, we chose an intermediate state pulse with a Gaussian beam profile and a linear phase along the radial coordinate. Their amplitude and phase are optimized to avoid ionization while back-propagating toward the position of the initial pulse (output of the laser), therefore preventing the potential divergence triggered by the nonlinear gain. The waveform obtained after backpropagation can be further approximated by an analytical expression, which can be characterized by a couple of control parameters. With the above forward and backward propagation of the intermediate state, the results of the numerical simulations relate the characteristics of the filament to the control parameters of the intermediate state and then to those of the initial pulse. Scaling laws are extracted by fitting the simulation results. Finally, a thorough forward propagation from the initial state to the final filament is performed to validate the scaling laws derived for the filament length as a function of the projection distance and the characteristics of the initial state.

II. NONLINEAR PROPAGATION OF A ULTRASHORT LASER PULSE IN AIR

Following Mlejnek *et al.* [32], we perform numerical simulations of the nonlinear propagation of an ultrashort laser pulse in air by solving an extended nonlinear Schrödinger equation (NLSE) for the envelope of the electric field coupled with a rate equation describing the generation of an electron plasma. The electric field $\boldsymbol{E}$ is assumed to propagate along the z-axis, to be linearly polarized along $\boldsymbol{e}_x$ and written by $\boldsymbol{E} = \mathcal{E}\exp(ik_0 z - i\omega_0 t)\boldsymbol{e}_x$, where ω_0 denotes the central frequency of the carrier wave and k_0 the corresponding wavenumber. The electric-field envelope $\mathcal{E}(r,t,z)$ satisfies

$$\partial_z \mathcal{E} = \frac{i}{2k_0}\Delta_\perp \mathcal{E} + iD(i\partial_t)\mathcal{E} + i\frac{\omega_0}{2cn_0}\frac{\mathcal{P}(\mathcal{E})}{\epsilon_0}, \tag{1}$$

where t refers to the local time within the pulse waveform. The transverse Laplacian $\Delta_\perp$ accounts for diffraction in the transverse plane, and is written as $\Delta_\perp = r^{-1}\partial_r(r\partial_r)$ under the assumption made throughout this paper, of beam cylindrical symmetry around the z axis. The operator $D(i\partial_t) = \sum_{n=2}^{+\infty}\frac{k_0^{(n)}}{n!}(i\partial_t)^n$ accounts for the effect of dispersion in the time domain and is easily calculated in the frequency domain as $\hat{D}(\omega) \equiv k(\omega) - k_0 - k_0'(\omega - \omega_0)$, where $k_0 \equiv k(\omega_0)$, while the dispersion in air is due to the frequency dependence of the refractive index $n(\omega)$, which is related to the wavenumber $k(\omega) = n(\omega)\omega/c$ and given by the relation established by Peck and Reeder [54]. The last term on the right-hand side of Eq. (1) denotes the nonlinear polarization

$$\mathcal{P}(\mathcal{E}) \equiv 2\epsilon_0 n_0(\Delta n(r,t,z) + i\kappa(r,t,z))\mathcal{E}(r,t,z) \tag{2}$$

describing the changes of refractive index Δn, due to optical Kerr effect and plasma defocusing, as well as nonlinear absorption with a coefficient κ, contributed by multiphoton absorption and plasma absorption,

$$\Delta n(r,t,z) = n_2\int_{-\infty}^{t} R(t-\tau)\mathcal{I}(r,\tau,z)d\tau - \frac{\sigma\omega_0\tau_c}{2k_0}\rho(r,t,z),$$
$$\kappa(r,t,z) = \frac{\sigma}{2k_0}\rho(r,t,z) + \frac{\beta_K}{2}\mathcal{I}^{K-1}(r,t,z). \tag{3}$$

The Kerr response function

$$R(t) = (1-f_R)\delta(t) + f_R\frac{\Gamma^2+\Omega^2}{\Omega}\exp(-\Gamma t)\sin(\Omega t) \tag{4}$$

encompasses the instantaneous electronic and delayed molecular rotational contributions, parametrized by a relative weight f_R for the delayed part with frequencies Γ and Ω. The quantity τ_c denotes the electron collision time entering in the cross section for inverse bremsstrahlung [55]

$$\sigma = \frac{k_0}{\rho_c}\frac{\omega_0\tau_c}{1+\omega_0^2\tau_c^2}, \tag{5}$$

where $\rho_c \equiv \omega_0^2\epsilon_0 m/e^2$ denotes the critical electron number density for an overdense plasma with respect to an electromagnetic radiation of frequency ω_0.

TABLE I. Parameters used for simulations of the propagation in air of a pulse at 800 nm.

Pulse energy (mJ)	10
θ (deg)	0.1, 0.125, 0.15, 0.175, 0.2
w_0 (mm)	5, 10, 15, 20
t_p (fs)	50
n_2 (m^2/W)	3.2×10^{-23}
f_R	0.5
Γ^{-1} (fs)	70
Ω (THz)	16
τ_c (fs)	350
E_g (eV)	12.1
K	8
$\beta^{(K)}$ (m^{13}/W^7)	1.83×10^{-120}
a (m^3/s)	5.0×10^{-13}

Evolution of the electron number density on the femtosecond time scale is mainly driven by multiphoton ionizations, our model also includes weaker cascade ionizations and radiative recombinations,

$$\partial_t \rho = \frac{\sigma}{E_g}\rho\mathcal{I} + \frac{\beta^{(K)}\mathcal{I}^K}{K\hbar\omega} - a\rho^2, \tag{6}$$

where E_g is the ionization potential and $\beta^{(K)}$ the K-photon absorption coefficient.

In our simulations, the electric field envelope of the intermediate state is Gaussian both in space and time, while the phase is linearly modulated in the radial direction, as obtained experimentally by transmitting a Gaussian pulse through an axicon with a cone angle θ,

$$\mathcal{E}(r,t,z_0) = \mathcal{E}_0 \exp\left(-\frac{r^2}{w_0^2} - \frac{t^2}{t_p^2} - ik_0 r\sin\theta\right). \tag{7}$$

The pulse duration $t_p = 50$ fs is fixed, and the central wavenumber $k_0 = 2\pi/\lambda_0$ corresponds to a central wavelength of $\lambda_0 = 800$ nm. The amplitude $\mathcal{E}_0 = \sqrt{2P_{\text{in}}/\pi w_0^2}$ is obtained by fixing w_0 and the input power P_{in} for a pulse energy of 10 mJ.

Table I summarizes the parameters used to solve the NLSE [Eq. (1)], in the both forward and backward directions with the initial conditions determined by the intermediate state given by Eq. (7). The critical power P_{cr} for self-focusing can be calculated to be about 3 GW.

Different pairs of parameters (w_0, θ) are chosen for the intermediate state, guided by the knowledge that (i) a linear propagation of the pulse [Eq. (7)] would result in a focal line extending over the Bessel zone of length $z_B \equiv w_0/\tan\theta$ [56] and (ii) a nonlinear propagation would lead to a filament that covers the Bessel zone with a more uniform intensity [38].

The choice of the pulse energy of the intermediate state ensures a negligible ionization for a reversely propagating pulse avoiding therefore an eventual divergence of the simulation [52]. Among nonlinear effects, only the Kerr nonlinearity is relevant during the backward propagation of the intermediate pulse.

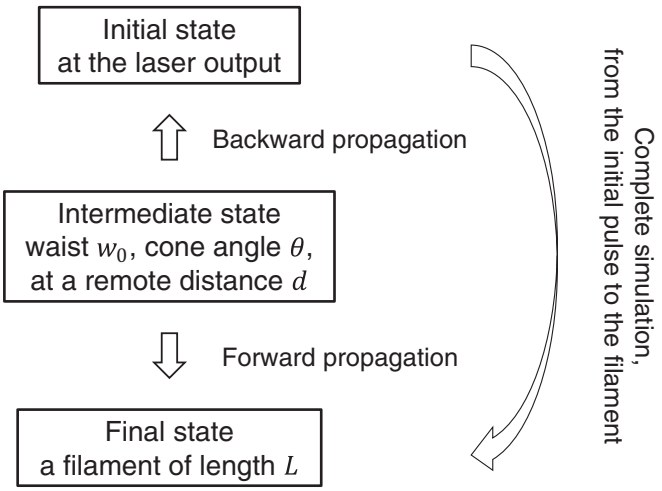

FIG. 1. Flowchart integrating of inverse design into the simulation of the evolution of a NIR ultrashort intense laser pulse into a filament.

III. REVERSE ENGINEERING THROUGH AN INTERMEDIATE STATE

The flowchart of the combination of inverse design and numerical simulation is shown in Fig. 1. The intermediate state is first forward propagated leading to a filament, accompanied by a plasma channel. Its backward propagation allows us to find the form of the initial pulse at the laser output capable of projecting such an intermediate state. After reversely engineering the wavefront of the initial pulse, a complete simulation is performed to investigate the relationship between initial pulse and the filament in order to verify the robustness of the method.

A. Generation of a filament together with the associated plasma channel with a controllable length

We first determine the conditions required to generate a filament in air with a plasma channel several meters long by modeling the nonlinear propagation of the intermediate state. The evolution of the field and the generation of a filament depend on the properties of the intermediate state, especially the spatial distribution of the intensity. Figure 2 presents a summary of the simulation results for the peak intensity of the filament and the peak electron number density in the plasma channel. They are obtained for cone angles θ ranging from 0.1 to 0.2 degrees and for beam widths w_0 ranging from 5 mm to 20 mm. The peak intensity is calculated by taking the maximum of $|\mathcal{E}(r,t,z)|^2$ at each propagation distance z and the electron density is extracted out by solving the rate equation governing the photoionization [see Eq. (6)]. Shown in Fig. 2(a) are results for a fixed cone angle $\theta = 0.15°$. With an increasing w_0, both the peak intensity and electron density decrease, while the lengths of the corresponding light and plasma channels increase. Results in Fig. 2(b) are obtained for different cone angles by keeping a constant $w_0 = 15$ mm. The peak intensity and electron number density grow with an increasing θ, while the channel lengths are reduced. The observed trends are determined by the spatial phase distribution

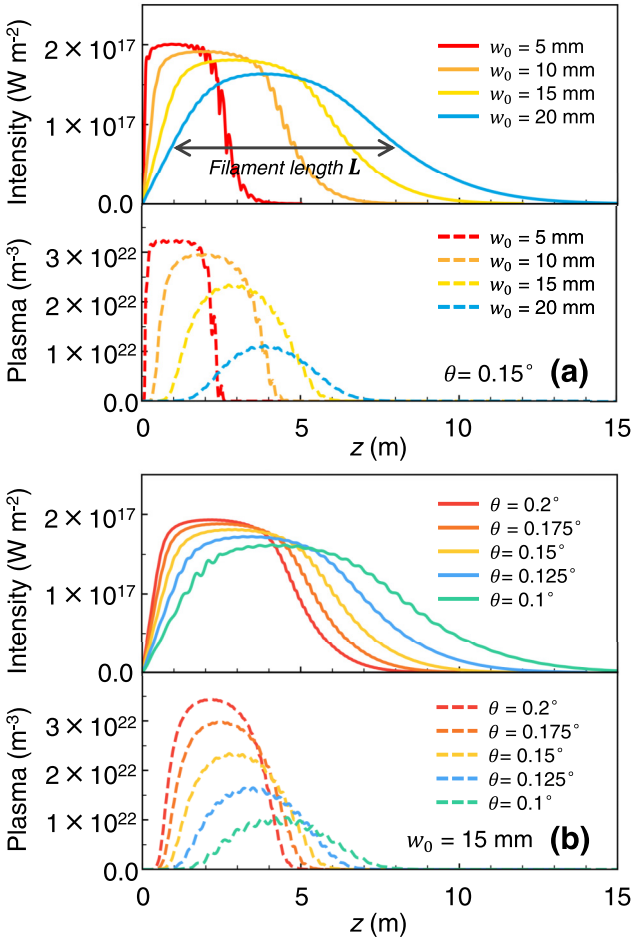

FIG. 2. Peak intensity and electron number density of a filament as functions of the propagation distance z. (a) for different beam waists w_0 of the intermediate pulse with a given cone angle $\theta = 0.15°$, and (b) for different cone angles θ with $w_0 = 15$ mm. The length of a filament L is extracted by measuring the full width at half maximum (FWHM) of the intensity curve.

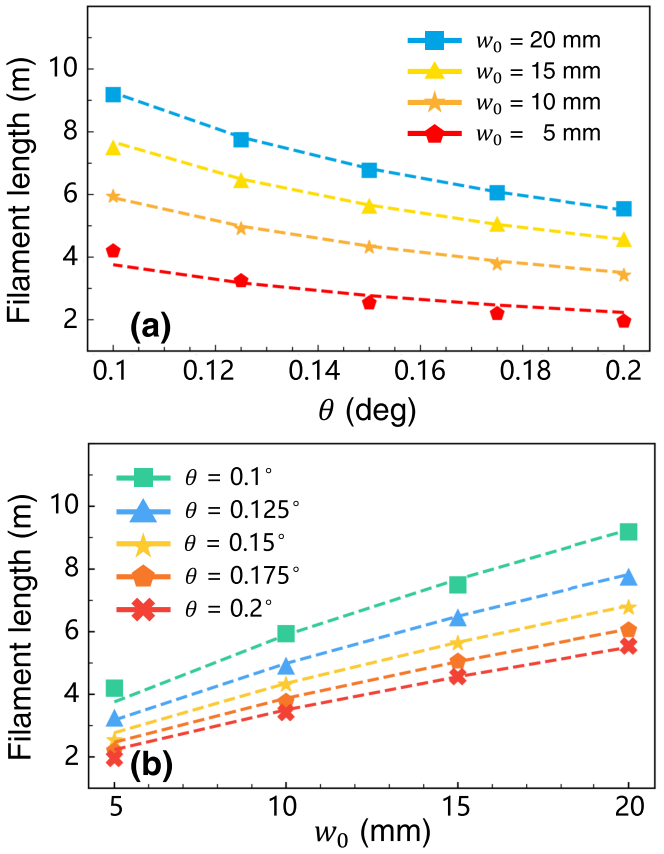

FIG. 3. Filament length L as a function of (a) the cone angle θ, and (b) the beam waist (w_0) of the intermediate state. The dashed lines represent the fits by the function given in Eq. (8).

of the intermediate pulse, which governs the conical energy flux sustaining the filament. As the waist w_0 increases, a larger energy reservoir surrounds the central core. In parallel, a smaller cone angle θ reduces the inward energy flow. The nonlinear propagation can be maintained for a longer distance due to the both effects. Note that in all simulation results, a single, continuous, and quite homogeneous filament with the associated plasma channel string is obtained. Periodic oscillations of a small amplitude appear, due to the interference between the conical and axial components of the beam and the interference induced by the nonlinear phase modulation.

Quantitatively, the length of a filament L is defined by the full width at half maximum (FWHM) of the peak intensity profile along the z axis [see Fig. 2(a)]. Filament lengths calculated from our simulation results are shown in Fig. 3 as a function of w_0 and θ. In our simulations, intensity clamping becomes one of the relevant effects flattening the profiles of the peak intensity along the z axis, as compared to the profile obtained with a linear propagation of a Bessel-Gauss beam, whose focal line scales as the Bessel zone $z_B = w_0/\tan\theta$. A fit of the simulation data results in a scaling law of the filament length L as a function of w_0 and θ,

$$L(w_0, \theta) = 136 \frac{\lambda_0^{0.35} w_0^{0.65}}{(\tan\theta)^{0.75}} \propto z_B^{0.75} / \hat{w}_0^{0.1}. \quad (8)$$

The dependence on the dimensionless beam waist $\hat{w}_0 \equiv w_0/\lambda_0$ and θ indicates that the filament length is expected to increase less fast than the Bessel range z_B, when w_0 increases or θ decreases. The scaling law of Eq. (8) provides therefore a practical way to precisely control the length of a filament, together with its related properties by the characteristics of the intermediate state.

B. Back propagation toward an initial state nearby the laser

To investigate the required initial pulse capable of projecting a Bessel-Gauss beam at a large distance, we propagate the intermediate pulse backward toward the laser and deduce the characteristics of the initial pulse nearby the laser. Since the intermediate pulse is chosen to have an intensity below the ionization threshold while possibly carrying a significant energy with a quite large beam waist, and a spatial phase gradient for a divergent back propagation, reverse solution is almost linear, except for a small contribution from optical Kerr effect. Figure 4 shows the simulation results of the amplitude and phase distributions of an initial pulse obtained at a distance d of 20 m upstream of the intermediate state. During the reverse propagation, the intermediate

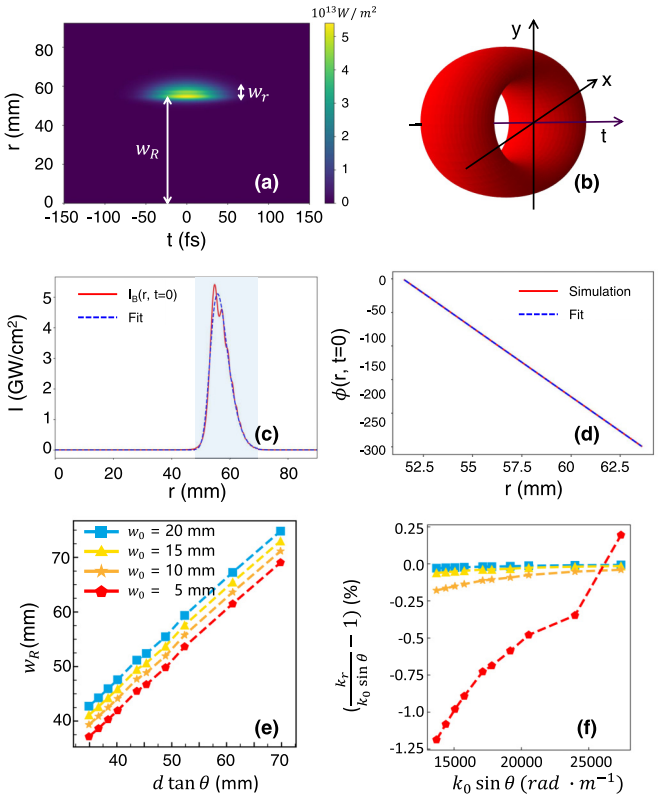

FIG. 4. Results of the reverse propagation of the intermediate pulse over a distance d of 20 m, with $\theta = 0.15°$, $w_0 = 10$ mm. (a) Intensity distribution of the resulted initial pulse $|\mathcal{E}(r, t, z = -d)|^2$ as a function of r and t. (b) Illustration of a torus pulse. (c) Intensity in the pulse center $|\mathcal{E}(r, t = 0, z = -d)|^2$ and a fit with Eq. (11). (d) Radial phase variation at the center of the pulse $\phi(r, t = 0)$ and its fit with a linear function. (e) Major radius of the initial torus pulse w_R as a function of $d \tan\theta$ for different w_0. (f) Comparison of the actual radial wavenumber k_r of the torus pulse and the projection of the central wavevector $k_0 \sin\theta$.

Bessel-Gauss pulse evolves into a torus-like pulse that can be considered as a Gaussian pulse with a ring beam profile [Figs. 4(a) and 4(b)]. The major and minor radii w_R, w_r of the ring depend on w_0 and θ. There is almost no change in the distribution of the electric field envelope along the time axis. The pulse remains Gaussian and its duration is nearly the same as that of the intermediate pulse of 50 fs. Dispersion in air is too weak to induce a significant pulse distortion over a distance of 20 m, the dispersive length in air for a 50 fs pulse being 62 m. For a larger propagation distance, dispersion can be compensated by prechirping the initial pulse. In this case, we can use a parabolic function to express the chirped temporal phase and a Gaussian function to express the amplitude when reversely propagating the wavefront. Along the radial axis, the electric field amplitude evolves into a ring beam [Fig. 4(c)] with a linear phase shift within the width of the ring, $\phi(r) = k_r + \phi_0$ as shown in Fig. 4(d).

The simulated values of w_R as a function of w_0 and θ are shown in Fig. 4(e). In the figure, we can see that the data can be well fitted by the relations derived by Gori *et al.* for the diffraction of a Bessel-Gauss beam [56], proving its validity

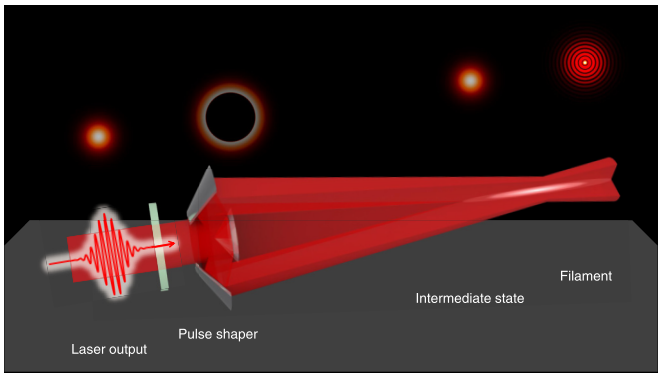

FIG. 5. Schematic representation of reverse engineering of a remote filament. Starting with a predefined intermediate state, the wavefronts after the pulse shaper are calculated by backward propagation. From the Gaussian pulse at the laser output, the required phase and amplitude modulation can be realized by a phase plate and axicon reflectors. The color plots show the evolution of the field from a Gaussian to a torus pulse through the pulse shaper, the projection of the torus pulse to a Gaussian beam passing through a remote virtual axicon, and finally its propagation in the form of a nonlinear Bessel-Gauss beam entering into the filamentation regime.

in the presence of a weak nonlinear effect,

$$w_R \sim d \tan(\theta). \tag{9}$$

At the same time, the simulations also show a good fit of the values of w_r by the diffraction of a Bessel-Gauss beam [56],

$$w_r \sim w_0 \sqrt{1 + d^2/{Z_R}^2}, \tag{10}$$

where w_0 is the beam waist at the intermediate state and $Z_R = \pi {w_0}^2/\lambda_0$ the Rayleigh length. In Fig. 4(f), the actual radial wavevectors k_r extracted from the simulations are compared with the projection of the central wavevector $k_0 \sin\theta$ according to the cone angle of the Bessel-Gauss beam. The result shows a relative difference within 2%, which confirms a quite good linear variation of the phase, similar to the intermediate state.

C. Projection of a torus pulse into a remote filament

The above simulation results suggest an implementation of the studied method to launch and control a filament at a remote distance. As shown in Fig. 5, an output pulse from a CPA laser with temporal and spatial Gaussian profiles, transmits first through a phase plate ensuring a linear radial phase modulation over the wavefront of the pulse. It is then reflected on an axicon mirror resulting in a pulse with a ring-formed beam profile. The latter propagates toward a ring mirror and is reflected onto the forward direction with a required convergence angle. At the same time, the reflectivity of the ring mirror is modulated in the radial direction so that when the ring-formed beam is reflected away from it, its intensity profile in the radial direction within the width of the ring is modulated according to the required profile. The ensemble of the phase plate, the axicon mirror and the ring mirror constitutes therefore a pulse shaper, which can transform a Gaussian pulse from a CPA laser into a torus pulse required for the projection of an

intermediate state of a Bessel-Gauss pulse and the subsequent formation of a filament.

For an easy implementation of the above conceptual arrangement, we neglect the small scale radial modulation of the intensity within the width of the ring beam profile as shown in Figs. 4(a) and 4(c). And the radial intensity distribution is approximated by a Gaussian profile centered at a major radius of w_R and having a e^{-1} half width of w_r. Later simulations will show the pertinence of such approximation with the fact that a similar filament can be formed when an actual radial intensity profile is replaced the above described Gaussian one. The initial pulse obtained by reverse engineering as shown in Figs. 4(a) and 4(c) is therefore approximated by an analytical expression,

$$\mathcal{E}_{\rm eng}(r,t) = A\exp\left(-\frac{(r-w_R)^2}{w_r^2} - (1+iC)\frac{t^2}{t_0^2} - ik_r r\right)\left[1+\mathrm{erf}\left(p\frac{(r-w_R)}{\lambda_0\sqrt{\hat{w}_r}}\right)\right], \tag{11}$$

where A is the amplitude determined by the pulse energy, $\mathrm{erf}(x)$ represents the error function, p is a fitting parameter, which can be approximated by $p \cong 0.028$ and $\hat{w}_r \equiv w_r/\lambda_0$. The chirp coefficient C is parametrized so as to compensate for dispersion during the projection stage to the intermediate state, i.e., $C = -d/Z_d$ where $Z_d = t_p^2/2k''$ denotes the dispersion length. The initial pulse duration can be modified accordingly to $t_0 = t_p\sqrt{1+d^2/Z_d^2}$. For $t_p = 50$ fs and $k'' = 0.2$ fs^2/cm, we find $Z_d = 62.5$ m, and for $d = 20$ m, we obtain $C = 0.32$ and $t_0 = 1.05t_p$. Such ideal torus pulse considered as the initial state of a complete forward propagation is therefore characterized by three parameters of w_R, w_r, and d, together with the characteristics of the pulse delivered by the CPA laser (pulse energy, pulse duration, and wavelength). Note that $k_r = k_0\sin\theta$, and θ can be further expressed as a function of w_R and d. Intensity distribution of an ideal torus pulse is shown in Fig. 6 for projecting at $d = 20$ m, an intermediate state with $\theta = 0.15^\circ$ and $w_0 = 10$ mm.

Starting the simulation from the torus pulse of Eq. (11) and propagating forward, the results confirm that the pulse is focused at the predefined projection distance d and further evolves into a filament with a length $L(w_R, w_r, d)$. It is therefore interesting to deduce the expression of $L(w_R, w_r, d)$ using the above deduced scaling law of $L(w_0, \theta)$ in Eq. (8) and those relating w_0 and θ to w_R, w_r, and d. Furthermore, using the scaling laws of Eqs. (9) and (10) confirmed by the results of the reverse simulation, we can relate the pair of control parameters of the intermediate state w_0 and θ to the characteristics of the ideal torus pulse of the initial state and the projection distance d,

$$\tan\theta = \frac{w_R}{d}, \tag{12}$$

$$w_0^2 = \frac{w_r^2}{2}\left(1+\sqrt{1-\frac{4d^2}{Z_r^2}}\right), \tag{13}$$

where $Z_r = \pi w_r^2/\lambda_0$ denotes the Rayleigh length constructed from w_r. Note that, Z_r must be greater than twice the projection distance to avoid reaching the diffraction limit. The scaling law for the filament length L as a function of the projection distance d and the torus pulse radii w_R and w_r can thus be deduced,

$$L(w_R, w_r, d) \approx \frac{51.6\,\lambda_0\left[\frac{Z_r^2}{w_r^2}\left(1+\sqrt{1-\frac{4d^2}{Z_r^2}}\right)\right]^{0.325}}{(w_R/d)^{0.75}}. \tag{14}$$

An end-to-end forward propagation simulation is then performed to calculate the filament length L for various combinations between w_R and w_r when d is fixed at 20 m. The obtained results are shown in Fig. 7 together with the plots of the scaling law of Eq. (14). A good agreement can be observed. This scaling law can thus be used to determine the parameters of the torus pulse of the initial state according to

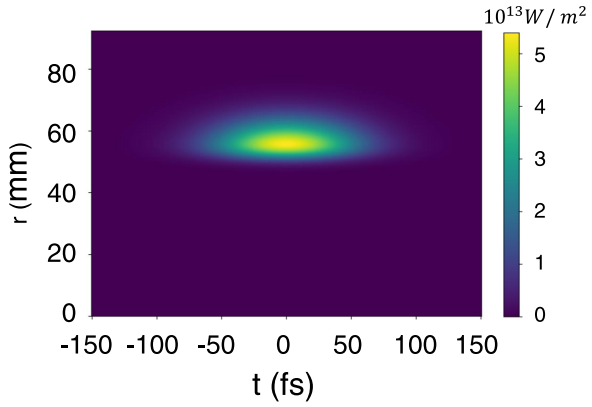

FIG. 6. Intensity of an ideal torus pulse as the initial state for projecting and a Bessel-Gauss beam intermediate state at a distance $d = 20$ m, with $\theta = 0.15^\circ$ and $w_0 = 10$ mm, the corresponding spatial and temporal phases are respectively linear and quadratic as described in the previous section.

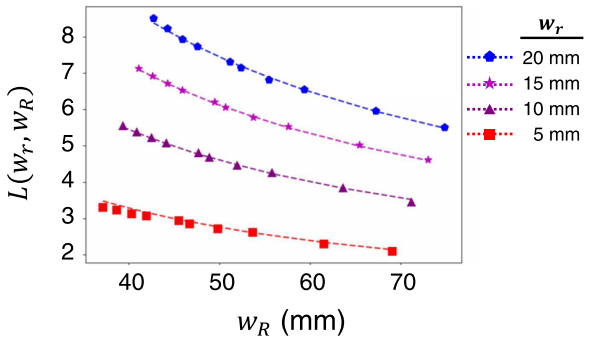

FIG. 7. Filament length as a function of major radius w_R of the torus pulse [see Eq. (11)] after forward propagation over $d = 20$ m. Dashed curves correspond to the fitting function given in Eq. (14) for different values of the minor radius w_r.

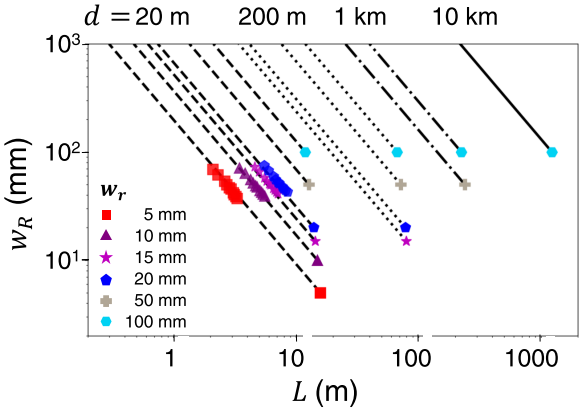

FIG. 8. Torus major radius w_R as a function of the filament length L, for various minor radius w_r and projection distances d up to 10 km. Each line corresponds to a fixed value of w_r and d.

the starting distance d and the length L of the filament that we want to generate. In practice, several pairs of (w_R, w_r) can be used to achieve the same filament project. For instance, the minor radius of the torus w_r can be chosen arbitrarily provided that the condition $Z_r > 2d$ is fulfilled, then requiring the major radius w_R to satisfy

$$w_R \approx 192\, d \left(\frac{\lambda_0}{L}\right)^{1.33} \left[\frac{Z_r^2}{w_r^2}\left(1+\sqrt{1-\frac{4d^2}{Z_r^2}}\right)\right]^{0.43}, \quad (15)$$

and the transverse wavenumber characterizing the radial spatial phase modulation is determined by $k_r = k_0 w_R/d$. Figure 8 shows the dependence of w_R upon the target filament length L for several values of d and w_r. The reduction of possible values of w_r as d increases is due to the threshold condition of $w_r > \sqrt{2d\lambda_0/\pi}$. The case of $w_R < w_r$ is also excluded. In the figure, we also plot the filament lengths resulted from the simulations for $d = 20$ m. We can see that longer filaments can be produced at a same projection distance by keeping w_R fixed and by increasing w_r (up to $w_r \approx w_R$). In addition, we can launch a filament of a given length to a larger distance by increasing w_R while keeping w_r fixed.

Finally, our simulations show that the larger the projection distance and the filament length are, the larger the values of w_R and w_r are required. For instance, projecting a 10-m-long filament to a distance of $d = 100$ m, requires a torus pulse with $w_R = 8.1$ cm and $w_r = 1$ cm (corresponding to a $\theta = 0.045°$). If the projection distance is increased to $d = 1$ km, w_r must be increased above the threshold value of ≈2.26 cm. Choosing $w_r = 6$ cm, a 10-m-long filament can be generated with a relatively large $w_R \approx 3.9$ m. Alternatively, with the other parameters ($w_r = 6$ cm, $d = 1$ km) kept unchanged, filaments with longer lengths of $L = 30$ m or $L = 100$ m can be generated with smaller w_R of respectively 91 cm or 18 cm, which remains still manageable with a tabletop laboratory optical arrangement.

IV. DISCUSSION

In our results, the simultaneous control of the filament length and projection distance relies on two key processes: (i) the focusing stage of the torus pulse into the intermediate Bessel-Gauss beam state is entirely achieved in a weakly nonlinear regime where the peak intensity remains below ionization threshold. (ii) The subsequent filamentation of the powerful Bessel-Gauss intermediate state is governed by the spontaneous generation of a propagation-invariant beam during its nonlinear propagation, previously identified as a nonlinear unbalanced Bessel beam [33–36]. As in previous experiments on long range filamentation, optical components of large size are required to reach long distances but the benefits of projecting a nonlinear Bessel beam lies in the simultaneous control of the filament length and projection distance. We discuss the main physical effects in each propagation stage.

During the first stage, the only nonlinear effect influencing the propagation is optical Kerr effect. Nonlinear losses are negligible as the highest peak intensity appearing at the projection distance for the intermediate state is chosen below ionization threshold, while allowing for the power of the beam to exceed the critical threshold for self-focusing. In this stage, the propagations in the forward and backward directions are essentially governed by diffraction and dispersion, making possible the semi-analytical derivation of the scaling laws (14) and (15) for the filament length, reflecting diffraction optics, and dispersion compensation of a prechirped pulse.

During the second propagation stage from the intermediate state to the filament, the prevailing physical effects in the formation of a homogeneous filament are diffraction, optical Kerr effect, and nonlinear losses. The intermediate state is organized as a conical wave, i.e., a beam whose spatial phase is set to drive an energy flux along the vertex of a cone. The linear propagation of this state would result in the formation of a Bessel beam profile in the focal Bessel zone, which can be described as a superposition of two balanced Hankel components, carrying along the cone vertex the same amount of energy in and out of the focal region [35]. When the intensity in the focal region exceeds ionization threshold, nonlinear losses generate an unbalance in the Hankel components as the energy conservation requires that the energy flux in the focal region must be equal to the sum of the energy losses in the hot core of the beam and the energy flux out of the focal region. Moreover, this unbalance was shown to characterize attractors of the dynamics of nonlinear Bessel beam propagation in a Kerr media with nonlinear losses, in the form of propagation-invariant solutions to the NLS equation called nonlinear unbalanced Bessel beams, which are supported by the inward energy flux until the energy reservoir is exhausted [35,36]. These solutions are stable in a large region of the parameter space and therefore propagate steadily, giving rise to the resulted homogeneous filaments. An unsteady propagation regime also exists, generally obtained for smaller cone angles than those we have considered, that would give rise to nonhomogeneous filaments. However, our results were limited to homogeneous filaments.

The simultaneous control of the length and projection distance of homogeneous filaments proposed in this paper is therefore only limited by two requirements: (i) avoid a strong self-focusing that would lead to ionization before the target position of the intermediate Bessel-Gauss beam and (ii)

avoid the unsteady regime for nonlinear unbalanced Bessel beams [36–38].

V. CONCLUSIONS

In conclusion, we have implemented inverse design in numerical simulation of the nonlinear propagation of a NIR intense femtosecond laser pulse in air. Starting from an intermediate state in the form of a Gaussian pulse with a Bessel-Gauss beam profile characterized by the waist w_0 and the cone angle θ, its propagation is simulated using the NLSE in the both forward and backward directions. In the forward direction, the intermediate pulse evolves into a filament with the associated plasma channel. The length of the filament L is found to be controlled by w_0 and θ. The intermediate pulse is then reversely propagated, showing the evolution of the beam profile into a torus structure with a linearly increasing radius as it approaches the CPA laser, which can deliver the pulse, situated at a distance of d from the intermediate state. The divergent backward propagation leads to a decrease of the intensity, avoiding ionization of the air molecules crossed by the pulse and potential divergences during reverse simulation. The obtained torus-like beam profile can be characterized by the major and minor radii w_R, w_r, as well as a linear radial phase. The both parameters of w_R and w_r are shown to be related to w_0, θ, and d. An end-to-end forward propagation simulation is thus performed from an ideal initial torus pulse to the final filament, confirming the validity of the pulse reverse engineering procedure. Scaling laws are extracted to express w_0 and θ as functions of w_R, w_r, and d, which in turn allows deducing a scaling law relating the filament length L to the projection distance d and the radii of the initial torus pulse w_R and w_r. A conceptual optical beam shaper, with a combination of a phase plate, an axicon reflector, and a ring mirror, is proposed to transform a Gaussian pulse at the output of a CPA laser into a torus pulse able to launch a Bessel filament at a remote distance. The quasilinear propagation of the initial torus pulse toward a virtual intermediate state of a Bessel-Gauss beam profile offers a large scalability of the projection distance d. An extrapolation of the numerical results obtained in this paper thus allows launching filaments of several tens of meters long at hundreds to thousands of meters in air for a large number of applications.

ACKNOWLEDGMENTS

We thank Beiyi Zhang for the assistance on the figures. Long Zou has been supported by the Zhiyuan Honors Doctoral Program of Shanghai Jiao Tong University.

[1] A. Braun, G. Korn, X. Liu, D. Du, J. Squier, and G. Mourou, Self-channeling of high-peak-power femtosecond laser pulses in air, Opt. Lett. **20**, 73 (1995).

[2] J. Kasparian, M. Rodriguez, G. Méjean, J. Yu, E. Salmon, H. Wille, R. Bourayou, S. Frey, Y.-B. André, A. Mysyrowicz, R. Sauerbrey, J.-P. Wolf, and L. Wöste, White-light filaments for atmospheric analysis, Science **301**, 61 (2003).

[3] A. Couairon and A. Mysyrowicz, Femtosecond filamentation in transparent media, Phys. Rep. **441**, 47 (2007).

[4] R. W. Boyd, *Nonlinear Optics* (Academic Press, New York, 2020).

[5] H. Wille, M. Rodriguez, J. Kasparian, D. Mondelain, J. Yu, A. Mysyrowicz, R. Sauerbrey, J. P. Wolf, and L. Wöste, Teramobile: A mobile femtosecond-terawatt laser and detection system, Eur. Phys. J. AP **20**, 183 (2002).

[6] S. L. Chin, H. L. Xu, Q. Luo, F. Théberge, W. Liu, J. F. Daigle, Y. Kamali, P. T. Simard, J. Bernhardt, S. A. Hosseini *et al.*, Filamentation "remote" sensing of chemical and biological agents/pollutants using only one femtosecond laser source, Appl. Phys. B **95**, 1 (2009).

[7] M. Petrarca, S. Henin, N. Berti, M. Matthews, J. Chagas, J. Kasparian, J.-P. Wolf, G. Gatti, G. Di Pirro, M.-P. Anania *et al.*, White-light femtosecond lidar at 100Â tw power level, Appl. Phys. B **114**, 319 (2014).

[8] J.-C. Diels, B. R., K. Stahlkopf, and X. M. Zhao, Lightning control with lasers, Sci. Am. **277**, 50 (1997).

[9] M. Rodriguez, R. Sauerbrey, H. Wille, L. Wöste, T. Fujii, Y.-B. André, A. Mysyrowicz, L. Klingbeil, K. Rethmeier, W. Kalkner *et al.*, Triggering and guiding megavolt discharges by use of laser-induced ionized filaments, Opt. Lett. **27**, 772 (2002).

[10] R. Ackermann, K. Stelmaszczyk, P. Rohwetter, G. Méjean, E. Salmon, J. Yu, J. Kasparian, G. Méchain, V. Bergmann, S. Schaper *et al.*, Triggering and guiding of megavolt discharges by laser-induced filaments under rain conditions, Appl. Phys. Lett. **85**, 5781 (2004).

[11] O. Graydon, Lightning control by lasers, Nat. Photonics **3**, 120 (2009).

[12] P. Walch, B. Mahieu, L. Arantchouk, Y.-B. André, A. Mysyrowicz, and A. Houard, Cumulative air density depletion during high repetition rate filamentation of femtosecond laser pulses: Application to electric discharge triggering, Appl. Phys. Lett. **119**, 264101 (2021).

[13] A. Houard, P. Walch, T. Produit, V. Moreno, B. Mahieu, A. Sunjerga, C. Herkommer, A. Mostajabi, U. Andral, Y.-B. André *et al.*, Laser-guided lightning, arXiv:2207.03769.

[14] Y. Brelet, A. Houard, G. Point, B. Prade, L. Arantchouk, J. Carbonnel, Y.-B. André, M. Pellet, and A. Mysyrowicz, Radiofrequency plasma antenna generated by femtosecond laser filaments in air, Appl. Phys. Lett. **101**, 264106 (2012).

[15] C. D'Amico, A. Houard, M. Franco, B. Prade, A. Mysyrowicz, A. Couairon, and V. T. Tikhonchuk, Conical Forward THz Emission from Femtosecond-Laser-Beam Filamentation in Air, Phys. Rev. Lett. **98**, 235002 (2007).

[16] Y. Chen, C. Marceau, W. Liu, Z.-D. Sun, Y. Zhang, F. Théberge, M. Châteauneuf, J. Dubois, and S. L. Chin, Elliptically polarized terahertz emission in the forward direction of a femtosecond laser filament in air, Appl. Phys. Lett. **93**, 231116 (2008).

[17] Z. Zhang, Y. Chen, S. Cui, F. He, M. Chen, Z. Zhang, J. Yu, L. Chen, Z. Sheng, and J. Zhang, Manipulation of polarizations for

broadband terahertz waves emitted from laser plasma filaments, Nat. Photonics **12**, 554 (2018).

[18] K. Stelmaszczyk, P. Rohwetter, G. Méjean, J. Yu, E. Salmon, J. Kasparian, R. Ackermann, J.-P. Wolf, and L. Wöste, Long-distance remote laser-induced breakdown spectroscopy using filamentation in air, Appl. Phys. Lett. **85**, 3977 (2004).

[19] P. Rohwetter, K. Stelmaszczyk, L. Wöste, R. Ackermann, G. Méjean, E. Salmon, J. Kasparian, J. Yu, and J.-P. Wolf, Filament-induced remote surface ablation for long range laser-induced breakdown spectroscopy operation, Spectrochim. Acta Part B: At. Spectrosc. **60**, 1025 (2005).

[20] S. Tzortzakis, D. Anglos, and D. Gray, Ultraviolet laser filaments for remote laser-induced breakdown spectroscopy (LIBS) analysis: Applications in cultural heritage monitoring, Opt. Lett. **31**, 1139 (2006).

[21] M. Rodriguez, R. Bourayou, G. Méjean, J. Kasparian, J. Yu, E. Salmon, A. Scholz, B. Stecklum, J. Eislöffel, U. Laux, A. P. Hatzes, R. Sauerbrey, L. Wöste, and J.-P. Wolf, Kilometer-range nonlinear propagation of femtosecond laser pulses, Phys. Rev. E **69**, 036607 (2004).

[22] M. Durand, A. Houard, B. Prade, A. Mysyrowicz, A. Durécu, B. Moreau, D. Fleury, O. Vasseur, H. Borchert, K. Diener *et al.*, Kilometer range filamentation, Opt. Express **21**, 26836 (2013).

[23] S. Eisenmann, E. Louzon, Y. Katzir, T. Palchan, A. Zigler, Y. Sivan, and G. Fibich, Control of the filamentation distance and pattern in long-range atmospheric propagation, Opt. Express **15**, 2779 (2007).

[24] G. Méchain, A. Couairon, Y.-B. André, C. D'Amico, M. Franco, B. Prade, S. Tzortzakis, A. Mysyrowicz, and R. Sauerbrey, Long-range self-channeling of infrared laser pulses in air: A new propagation regime without ionization, Appl. Phys. B **79**, 379 (2004).

[25] G. Méchain, C. D'Amico, Y.-B. André, S. Tzortzakis, M. Franco, B. Prade, A. Mysyrowicz, A. Couairon, E. Salmon, and R. Sauerbrey, Range of plasma filaments created in air by a multi-terawatt femtosecond laser, Opt. Commun. **247**, 171 (2005).

[26] G. Méchain, G. Méjean, R. Ackermann, P. Rohwetter, Y.-B. André, J. Kasparian, B. Prade, K. Stelmaszczyk, J. Yu, E. Salmon *et al.*, Propagation of fs TW laser filaments in adverse atmospheric conditions, Appl. Phys. B **80**, 785 (2005).

[27] A. Couairon, M. Franco, G. Méchain, T. Olivier, B. Prade, and A. Mysyrowicz, Femtosecond filamentation in air at low pressures: Part I: Theory and numerical simulations, Opt. Commun. **259**, 265 (2006).

[28] G. Méchain, T. Olivier, M. Franco, A. Couairon, B. Prade, and A. Mysyrowicz, Femtosecond filamentation in air at low pressures. Part II: Laboratory experiments, Opt. Commun. **261**, 322 (2006).

[29] A. A. Ionin, N. G. Iroshnikov, O. G. Kosareva, A. V. Larichev, D. V. Mokrousova, N. A. Panov, L. V. Seleznev, D. V. Sinitsyn, and E. S. Sunchugasheva, Filamentation of femtosecond laser pulses governed by variable wavefront distortions via a deformable mirror, J. Opt. Soc. Am. B **30**, 2257 (2013).

[30] D. V. Apeksimov, Y. E. Geints, A. A. Zemlyanov, A. M. Kabanov, V. K. Oshlakov, A. V. Petrov, and G. G. Matvienko, Controlling TW-laser pulse long-range filamentation in air by a deformable mirror, Appl. Opt. **57**, 9760 (2018).

[31] A. C. Englesbe, Z. He, J. A. Nees, A. G. Thomas, A. Schmitt-Sody, and K. Krushelnick, Control of the configuration of multiple femtosecond filaments in air by adaptive wavefront manipulation, Opt. Express **24**, 6071 (2016).

[32] M. Mlejnek, E. M. Wright, and J. V. Moloney, Dynamic spatial replenishment of femtosecond pulses propagating in air, Opt. Lett. **23**, 382 (1998).

[33] A. Dubietis, E. Gaižauskas, G. Tamošauskas, and P. Di Trapani, Light Filaments without Self-Channeling, Phys. Rev. Lett. **92**, 253903 (2004).

[34] A. Dubietis, E. Kučinskas, G. Tamošauskas, E. Gaižauskas, M. A. Porras, and P. Di Trapani, Self-reconstruction of light filaments, Opt. Lett. **29**, 2893 (2004).

[35] M. A. Porras, A. Parola, D. Faccio, A. Dubietis, and P. Di Trapani, Nonlinear Unbalanced Bessel Beams: Stationary Conical Waves Supported by Nonlinear Losses, Phys. Rev. Lett. **93**, 153902 (2004).

[36] M. A. Porras, C. Ruiz-Jiménez, and J. C. Losada, Underlying conservation and stability laws in nonlinear propagation of axicon-generated bessel beams, Phys. Rev. A **92**, 063826 (2015).

[37] P. Polesana, A. Couairon, D. Faccio, A. Parola, M. A. Porras, A. Dubietis, A. Piskarskas, and P. Di Trapani, Observation of Conical Waves in Focusing, Dispersive, and Dissipative Kerr Media, Phys. Rev. Lett. **99**, 223902 (2007).

[38] P. Polesana, M. Franco, A. Couairon, D. Faccio, and P. Di Trapani, Filamentation in Kerr media from pulsed Bessel beams, Phys. Rev. A **77**, 043814 (2008).

[39] P. Polynkin, M. Kolesik, A. Roberts, D. Faccio, P. Di Trapani, and J. Moloney, Generation of extended plasma channels in air using femtosecond bessel beams, Opt. Express **16**, 15733 (2008).

[40] S. Akturk, B. Zhou, M. Franco, A. Couairon, and A. Mysyrowicz, Generation of long plasma channels in air by focusing ultrashort laser pulses with an axicon, Opt. Commun. **282**, 129 (2009).

[41] M. S. Mills, M. Kolesik, and D. N. Christodoulides, Dressed optical filaments, Opt. Lett. **38**, 25 (2013).

[42] M. Scheller, M. S. Mills, M.-A. Miri, W. Cheng, J. V. Moloney, M. Kolesik, P. Polynkin, and D. N. Christodoulides, Externally refuelled optical filaments, Nat. Photonics **8**, 297 (2014).

[43] M. K. Bhuyan, F. Courvoisier, P. A. Lacourt, M. Jacquot, R. Salut, L. Furfaro, and J. M. Dudley, High aspect ratio nanochannel machining using single shot femtosecond Bessel beams, Appl. Phys. Lett. **97**, 081102 (2010).

[44] C. Vetter, R. Giust, L. Furfaro, C. Billet, L. Froehly, and F. Courvoisier, High aspect ratio structuring of glass with ultrafast bessel beams, Materials **14**, 6749 (2021).

[45] V. Jukna, C. Milián, C. Xie, T. Itina, J. Dudley, F. Courvoisier, and A. Couairon, Filamentation with nonlinear Bessel vortices, Opt. Express **22**, 25410 (2014).

[46] K. Dota, A. Pathak, J. A. Dharmadhikari, D. Mathur, and A. K. Dharmadhikari, Femtosecond laser filamentation in condensed media with bessel beams, Phys. Rev. A **86**, 023808 (2012).

[47] M. K. Bhuyan, P. K. Velpula, J. P. Colombier, T. Olivier, N. Faure, and R. Stoian, Single-shot high aspect ratio bulk nanostructuring of fused silica using chirp-controlled ultrafast laser Bessel beams, Appl. Phys. Lett. **104**, 021107 (2014).

[48] F. Courvoisier, R. Stoian, and A. Couairon, [invited] Ultrafast laser micro- and nano-processing with nondiffracting and

curved beams: Invited paper for the section : Hot topics in ultrafast lasers, Opt. Laser Technol. **80**, 125 (2016).

[49] P. Panagiotopoulos, P. Whalen, M. Kolesik, and J. V. Moloney, Super high power mid-infrared femtosecond light bullet, Nat. Photonics **9**, 543 (2015).

[50] S. Tochitsky, E. Welch, M. Polyanskiy, I. Pogorelsky, P. Panagiotopoulos, M. Kolesik, E. M. Wright, S. W. Koch, J. V. Moloney, J. Pigeon, and C. Joshi, Megafilament in air formed by self-guided terawatt long-wavelength infrared laser, Nat. Photonics **13**, 41 (2019).

[51] N. Vansteenkiste, P. Vignolo, and A. Aspect, Optical reversibility theorems for polarization: Application to remote control of polarization, J. Opt. Soc. Am. A **10**, 2240 (1993).

[52] N. Berti, W. Ettoumi, J. Kasparian, and J.-P. Wolf, Reversibility of laser filamentation, Opt. Express **22**, 21061 (2014).

[53] N. Berti, W. Ettoumi, S. Hermelin, J. Kasparian, and J.-P. Wolf, Nonlinear synthesis of complex laser waveforms at remote distances, Phys. Rev. A **91**, 063833 (2015).

[54] E. R. Peck and K. Reeder, Dispersion of air, J. Opt. Soc. Am. **62**, 958 (1972).

[55] M. D. Feit and J. A. Fleck, Effect of refraction on spot-size dependence of laser-induced breakdown, Appl. Phys. Lett. **24**, 169 (1974).

[56] F. Gori, G. Guattari, and C. Padovani, Bessel-Gauss beams, Opt. Commun. **64**, 491 (1987).